nature communications

Article

https://doi.org/10.1038/s41467-025-65531-3

Mesh-like structure integrated core-shell-shell nanocomposites for enhanced stability and performance in carbon capture

Received: 21 October 2024

Accepted: 17 October 2025

Published online: 26 November 2025

Check for updates

Sizhuo Yang[1,8], Haiyan Mao[2,8], Chaochao Dun[1], Jianfang Liu[1], Kaipeng Hou[3], Angela Cai[2], Jing Wang[2], Jane K. J. Lee[4], Donglin Li[2], Hao Lyu[5], Zhouyi Chen[2], Xudong Lv[6], Hao Zhuang[6], Xueer Xu[2], Xueli Zheng[2], Gang Ren[1], Jeffrey A. Reimer[6,7] ✉, Yi Cui[2] ✉ & Jeffrey J. Urban[1] ✉

Carbon capture is essential for mitigating climate change, yet most sorbents struggle to combine high capacity with chemical stability. Here we report core-shell-shell (CSS) nanocomposites that integrate adsorption efficiency with exceptional robustness. The design couples a metal-organic framework (MOF) core, which enriches local CO_2 concentration, with a polyamine shell that is reorganized into a porous, ordered network through entanglement with an outer covalent organic framework (COF) shell. This hierarchical architecture enables dual amine functionalization via sequential "click" and Schiff-base reactions, achieving a CO_2 uptake of 3.4 mmol g^{-1} at 1 bar. The COF outer layer also acts as a protective barrier, suppressing humidity interference and doubling cycling stability under simulated flue gas. Remarkably, the nanocomposites maintain structural integrity after one week in strongly acidic (3 M HNO_3) or basic (NaOH, pH=14) environments, underscoring their chemical resilience. By uniting high capacity, cycling durability, and environmental tolerance, this CSS strategy offers a versatile platform for next-generation carbon capture materials.

Rising atmospheric carbon dioxide (CO_2) levels are considered a contributing factor to global warming and environmental challenges[1,2]. Consequently, carbon capture and sequestration (CCS) are seen as a powerful strategy to mitigate greenhouse gas emissions and combat climate change. Current CCS initiatives can capture 49 Mt (million tonnes) of CO_2 annually[3], which is significantly below the 7.6 Gtpa (gigatonnes per annum) target of the Paris Agreement, as indicated by the International Energy Agency (IEA)[4]. The high costs, particularly for CO_2 capture, which constitute up to 75% of the overall CCS expenses[5], are major obstacles to its broader implementation. Therefore, the development of cost-effective and energy-efficient decarbonization materials while maintaining their optimal performance is a top priority[6].

Amine-functionalized solid sorbents are emerging as a leading solution for next-generation carbon capture technology, addressing the limitations of aqueous amines, such as high energy requirements, amine degradation, and environmental hazards[7–9]. However, conventional amine-functionalized sorbents such as zeolites, silicas, and activated carbons are limited by their low amine group density and lack of structural design, leading to insufficient CO_2 capture

[1]The Molecular Foundry, Lawrence Berkeley National Laboratory, Berkeley, CA 94720, USA. [2]Department of Materials Science and Engineering, Stanford University, Stanford, CA 94305, USA. [3]Department of Chemistry, University of California, Berkeley, Berkeley, CA 94720, USA. [4]Department of Structural Biology, Stanford University, Stanford, CA 94720, USA. [5]Department of Chemical Engineering, Stanford University, Stanford, CA 94720, USA. [6]Department of Chemical and Biomolecular Engineering, University of California, Berkeley, CA 94720, USA. [7]Materials Sciences Division, Lawrence Berkeley Laboratory, Berkeley, CA 94720, USA. [8]These authors contributed equally: Sizhuo Yang, Haiyan Mao. ✉e-mail: reimer@berkeley.edu; yicui@stanford.edu; jjurban@lbl.gov

capacities[10–12]. This necessitates precise functionalization to boost their carbon capture performance. Porous organic frameworks, notably metal organic frameworks (MOFs)[13,14] and covalent organic frameworks (COFs)[15], are emerging as promising alternatives. Their inherent porosity and structural variety enable the tailoring of pore walls at the molecular level, thereby enhancing carbon capture capabilities. Amine-functionalized MOFs (see Supplementary Tables 1 for more details), for instance, have shown excellent CO_2 capture ability in flue gas, benefiting from the cooperative effect between the amine groups and the metal centers, with a CO_2 adsorption capacity up to 4.3 mmol g^{-1}[16,17]. Nevertheless, MOFs often face challenges such as low stability, short lifetime, and poor selectivity, particularly in the presence of H_2O[18–20]. In contrast, COFs exhibit increased stability under extreme conditions due to their robust covalent bonds, although their CO_2 adsorption capacity typically remains lower, with the top-performing COFs reaching around 2.7 mmol g^{-1}[21,22]. Thus, innovative approaches are needed to improve the overall performance of these materials and mitigate their current disadvantages.

Herein, we developed CSS MOF-COF nanocomposites enriched with a high density of amines, establishing a robust platform for CO_2 capture. This design strategically integrates MOF nanoparticles during COF synthesis, enabling independent optimization of the inner MOF core and the outer COF shells. Through "click" and Schiff-base reactions, molecular-level engineering of pore walls is achieved via covalent bonding. The cooperation between bridging polyethyleneimine (PEI) and COFs drives the formation of a mesh-like interface shell that anchors a protective COF outer layer while introducing additional CO_2 adsorption sites. This design significantly enhances CO_2 adsorption capacity and chemical stability. Moreover, the CSS structure serves as an effective diffusion barrier against water vapor[21,23,24], effectively mitigating the adverse effects of humidity on CO_2 adsorption. Comprehensive characterization of the PEI-modified CSS nanocomposites was conducted using cryo-electron microscopy (cryo-EM), Fourier transform infrared (FT-IR), solid-state nuclear magnetic resonance (NMR) spectroscopy, and density functional theory (DFT) calculations, elucidating the stability of chemisorbed CO_2 during adsorption-desorption cycles. Evaluations of adsorption kinetics, cycling stability, and regeneration energy further demonstrate the potential of CSS nanocomposites as advanced materials for carbon capture applications.

Results and discussion

Synthesis and characterization of CSS nanocomposites

To address the challenge of competitive adsorption between water and CO_2 in amine-appended MOFs, we developed a CSS structure, employing COFs as effective diffusion barriers to water vapor, thereby minimizing the negative impact of humidity. As illustrated in Fig. 1a, $[Zr_6O_4(OH)_4(BTC)_2(HCOO)_6]$ (BTC: 1,3,5-benzenetricarboxylate), or MOF-808, was chosen as the core for its excellent thermal and air stability and synthesized following a previously reported protocol[25]. The shell comprises an imine-linked TPB-DMTP COF (TPB: 1,3,5-triphenylbenzene; DMTP: 2,5-dimethoxyterephthaldehyde), selected for its high stability even under harsh chemical conditions[26]. During the self-assembly process, a mesh-like polyamine shell forms at the MOF interface through synergistic interactions, where crystalline COF become covalently bonded and intricately interwoven with the polyamine. This transformation from dense packing into a porous, well-organized mesh architecture significantly enhances CO_2 adsorption capacity while also creating a robust substrate to support the continued growth and stabilization of the protective COF shell. The COF shell was further functionalized with terminal aldehydes via a "click" reaction (Fig. 1b), followed by a Schiff-base reaction under mild conditions (Fig. 1b) to achieve maximum amine functionalization. This design ensures robust covalent bonding throughout the structure, effectively preventing amine leaching and maintaining high adsorption performance over time.

The CSS structure was systematically characterized to confirm its composition and stability. X-ray photoelectron spectroscopy (XPS) depth profiling of the N 1*s* spectra (Supplementary Fig. 1) revealed distinct chemical environments for the polyamine and COF shells, with peak shifts observed as the etching depth increased. High-angle annular dark-field (HAADF) transmission electron microscopy (TEM) and energy-dispersive spectrometry (EDS) mapping (Fig. 2e and Supplementary Fig. 2) confirmed the uniform COF coating on the surface of octahedral MOF crystals. To avoid beam damage during analysis, cryo-electron microscopy (cryo-EM) (Fig. 2d) was employed, revealing highly crystalline domains with d-spacings of ~2.11 and 3.21 nm, corresponding to the (100) planes of the MOF core and COF shell, respectively. Additionally, powder X-ray diffraction (PXRD) confirmed the overall crystallinity of the CSS nanocomposites, showing excellent agreement between experimental data and simulated patterns[25,26] (Fig. 2a and Supplementary Fig. 3). Thermogravimetric analysis (TGA) (Supplementary Figs. 4–6) demonstrated the enhanced thermal stability of CSS-PEI, which resisted amine loss up to ~390 °C, compared to MOF-808-PEI, which began losing amine at ~290 °C. This result highlights the improved stability imparted by covalent bonding within the CSS structure. Furthermore, no amine leaching was observed in the ^1H NMR spectrum of CSS-PEI after immersion in D_2O, whereas MOF-808-PEI exhibited significant leaching under the same conditions (Supplementary Fig. 7), confirming the superior stability of CSS-PEI in aqueous environments. As illustrated in Fig. 3d, adjusting the ratio of the COF edge ligands 2,5-bis(2-propynyloxy)terephthalaldehyde (BPTA) and 2,5-dimethoxyterephthalaldehyde (DMTP) enabled the synthesis of nanocomposites with gradient shell functionalities, denoted as CSS-*X*% (where *X* represents the percentage of functional groups, either of −C≡CH or of PEI). This tunability enhances the functional versatility of the CSS nanocomposites for targeted applications.

To optimize CO_2 adsorption capacity, dual amine adsorption sites were introduced into the CSS nanocomposites through a sequential growth strategy combining click chemistry and Schiff-base reactions (Fig. 1a). The successful modification of MOF-808 with polyethylenimine (PEI) was confirmed by FT-IR spectroscopy (Supplementary Fig. 8), as evidenced by the N-H stretch observed at 3200–3500 cm^{-1}. Additionally, the FT-IR spectra of CSS-C≡CH (Fig. 2b) displayed characteristic C≡CH stretching modes at 2120 cm^{-1} and 3300 cm^{-1}, confirming the formation of the COF shell (Supplementary Figs. 9–10). After the click reaction, FT-IR spectra of CSS-CHO (Fig. 2b) revealed the disappearance of C≡CH stretching, accompanied by the emergence of C=O stretching at 1723 cm^{-1} and N=N stretching at ~2800 cm^{-1}, indicating the completion of the linkage modification. Subsequent PEI functionalization was verified by the disappearance of C=O stretching and an increase in amino signal intensity in the FT-IR spectra of CSS-PEI (Fig. 2b), confirming the successful amine integration within the CSS nanocomposites.

Cross-polarization magic-angle spinning (CP-MAS) ^{13}C solid-state NMR spectra further validated the structural functionalization. As shown in Fig. 2c, the spectra of COF-C≡CH, COF-PEI and CSS-PEI were collected, where the signal at 70–85 ppm (assigned to the alkyne C) in COF-C≡CH disappeared following PEI incorporation in COF-PEI. In contrast, the signals at 40–60 ppm (assigned to aliphatic C atoms of PEI) were evident in COF-PEI. Similar peak changes were observed in CSS-PEI, indicating the successful incorporation of PEI into the composite structure. Notably, the aromatic ring signals (109–160 ppm) of CSS nanocomposites were mostly unaltered, suggesting that the overall CSS structure was preserved after amine installation. Both CSS nanocomposites exhibited permanent porosity, as evidenced by type IV isotherms obtained from N_2 sorption experiments at 77 K (Supplementary Figs. 11–14 and Table 4). The Brunauer–Emmett–Teller (BET)

https://doi.org/10.1038/s41467-025-65531-3

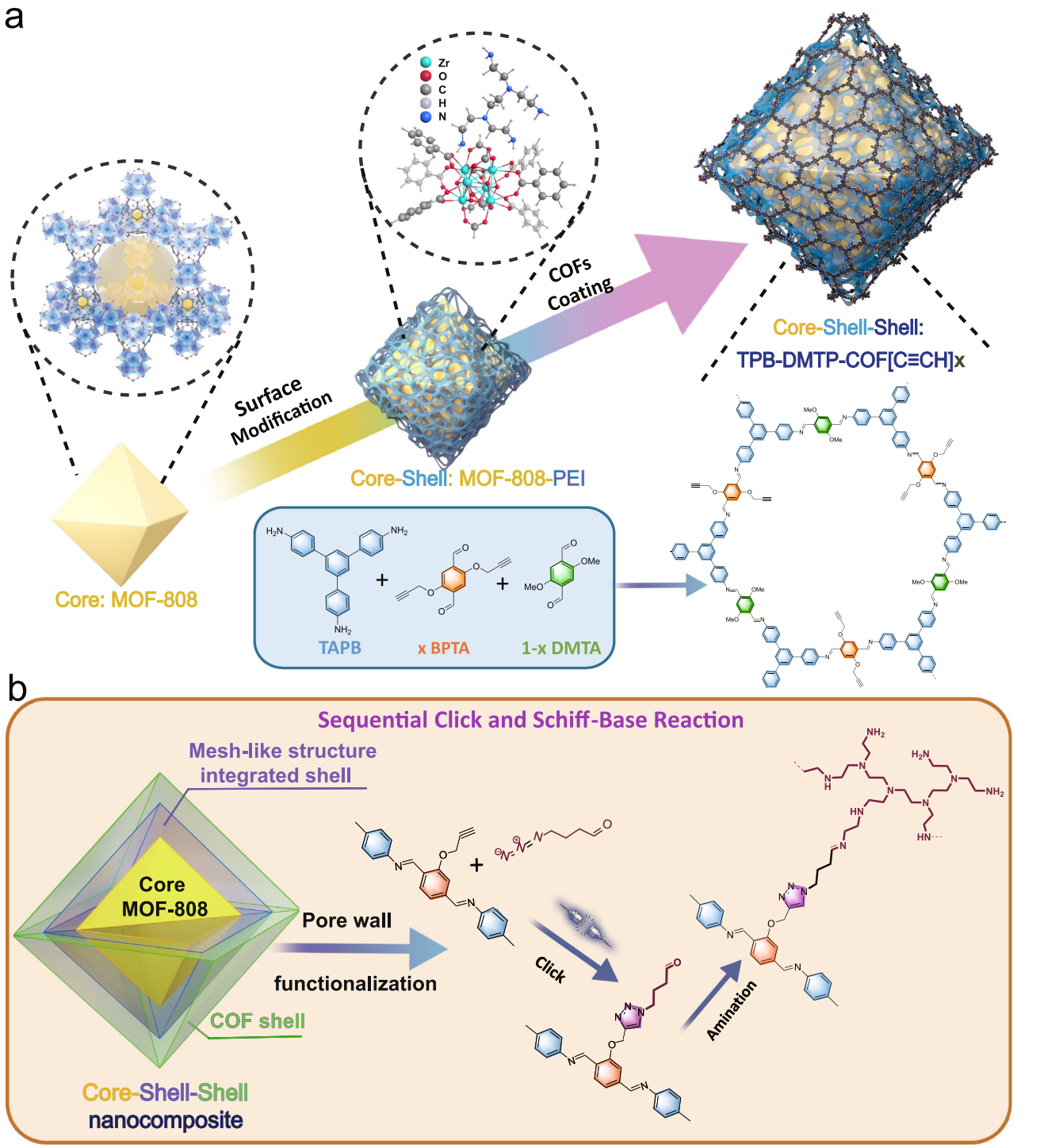

Fig. 1 | Design strategy and synthesis of CSS nanocomposites. a Synthetic scheme for constructing mesh-like CSS nanocomposites. MOF-808 serves as the core, while TPB-DMTP-COF[C≡CH]$_x$ forms the outer shell. Zr atoms are represented as blue polyhedral or spheres; all other atoms are represented as spheres (C, gray; O, red; N, dark blue; H, white). **b** Amine installation of CSS nanocomposites. Through a sequential "click" and Schiff-base reaction, polyamine is covalently grafted onto the backbone of the COF shell, yielding CSS-PEI.

surface area of the CSS-CHO and CSS-100% was calculated to be 808 and 412 $m^2 g^{-1}$, with a decrease of average pore size from 1.3 to 0.96 nm, as simulated by quenched solid density functional theory (QSDFT). This reduction was attributed to framework disorder during conversion and the flexible nature of incorporated PEI within pore channels.

To further elucidate the covalent and non-covalent interactions (NCIs) within the nanocomposite, DFT modeling was employed. Figure 3c, d illustrated the DFT calculated structure of MOF-808-PEI at the B3LYP-GD3BJ/6-31 G(d), LANL2DZ(Zr) level, together with optimized fragments of the individual components (Supplementary Figs. 34–37), including the COF-PEI shell. The PEI molecules were positioned along the COF edges with an average distance of 13.056 Å (Fig. 3d) through -C=N- covalent bonds. To gain more insight into the nature of intermolecular interactions, an independent gradient model based on Hirshfeld partition (IGMH) analysis (Fig. 3b) was performed, which revealed that van der Waals interactions (green regions) dominated the interplay between MOF-808 and PEI, with

https://doi.org/10.1038/s41467-025-65531-3

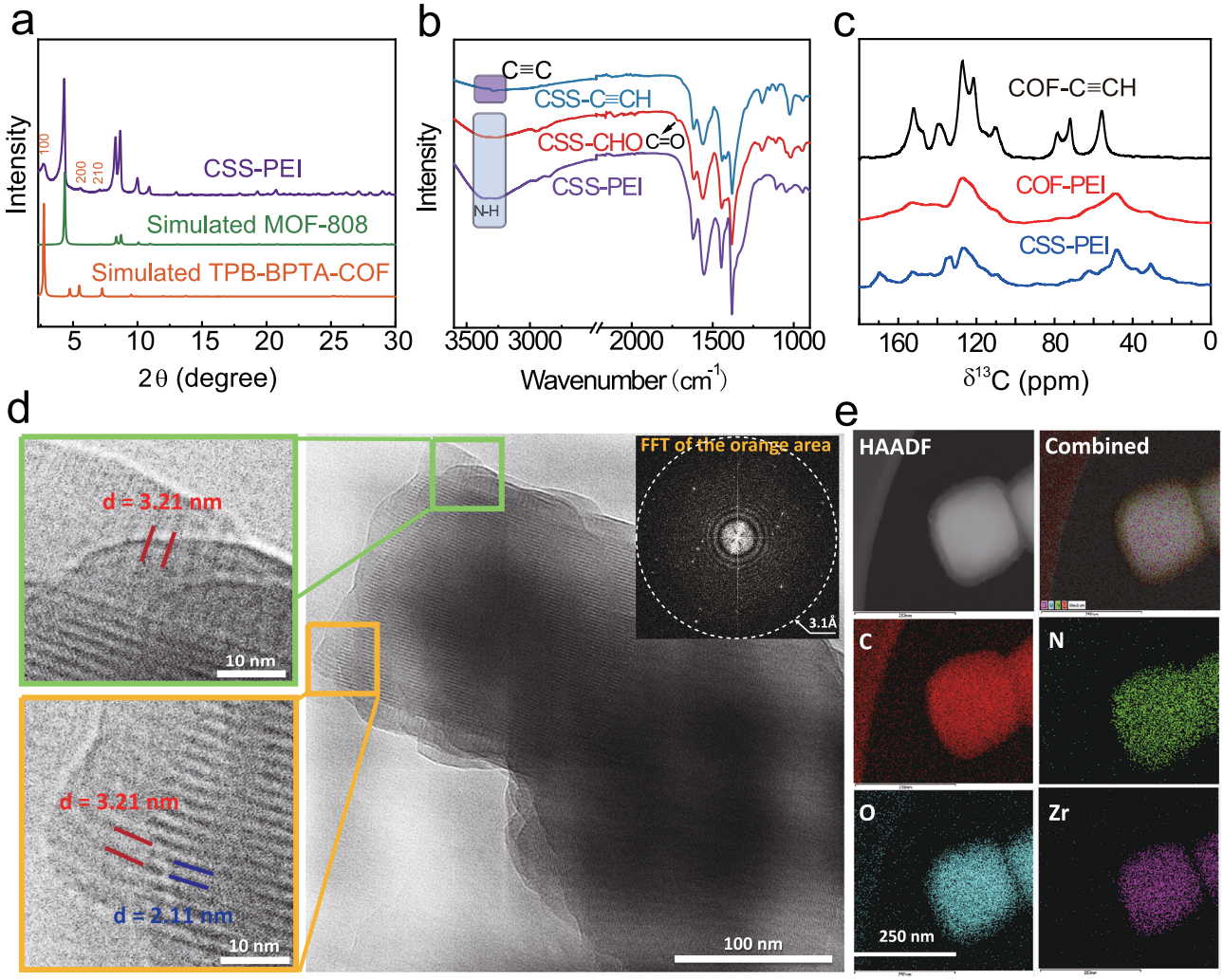

Fig. 2 | Structural characterization of CSS nanocomposites. a Experimental and simulated PXRD patterns of CSS-PEI, MOF-808 and TPB-BPTA-COF. **b** FT-IR of CSS-C≡CH, CSS-CHO and CSS-PEI. **c** Cross-polarized ^{13}C MAS NMR spectra of COF-C≡CH, COF-PEI and CSS-PEI. **d** Cryo-EM of CSS-PEI; the inset shows the FFT of the highlighted orange area, where distinct diffraction spots confirm crystalline order. The outermost diffraction spot corresponds to an interplanar spacing of ~3.1 Å, demonstrating that the cryo-EM image provides near-atomic resolution. **e** HAADF and corresponding EDS mapping of CSS-PEI.

strong hydrogen bonding (blue regions) and steric repulsion (red regions) also contributing, demonstrating the intricate interactions within the nanocomposite framework.

CO_2 adsorption performance and pore structure effects

Single-component CO_2 adsorption and desorption isotherms were measured at 25 °C (~298 K) for all obtained MOF-808-amine samples. Among the small-chain polyamines (Fig. 3a), including 2-Methylpentamethylene diamine (2-MPDA), Diethylenetriamine (DETA), N,N′-(ethane-1,2-diyl)bis(propane-1,3-diamine) (Tetraamine-323) and N,N′-(propane-1,3-diyl)bis(propane-1,3-diamine) (Tetraamine-333), MOF-808-diamine emerged as the best-performing material, achieving a CO_2 adsorption capacity close to 3 mmol g^{-1} at 1 bar (Fig. 4a). In contrast, MOF-808-PEI shows CO_2 capacity around 2.3 mmol g^{-1} at 1 bar (Fig. 4a and Supplementary Fig. 15). However, upon assembly with a COF shell, the CO_2 capacity of CSS-diamine decreased (Supplementary Fig. 16), mainly attributed to the limited amine density after multiple modification steps. Consequently, PEI was chosen as the final bridging composition for CSS synthesis. Despite having the lower surface area after amine installation, CSS-PEI exhibited the highest CO_2 adsorption capacity across the entire pressure range compared to MOF-808-PEI and COF-PEI (Fig. 4b). This observation can be attributed to the high density of amine from the dual adsorption sites in CSS-PEI nanocomposites. Additionally, the integration of bridging PEI with COF operates cooperatively, with the crystalline order of the COF guiding the formation of a mesh-like PEI interface shell, transforming it from a densely packed structure into a well-organized porous configuration with optimized spatial arrangement. This is confirmed by the pore size distribution, as shown in Supplementary Fig. 17, where additional micropores (<2 nm) were observed for CSS composites. This porous shell positively contributes to CO_2 adsorption, as evidenced by the CO_2 adsorption isotherm showing that CSS-CHO exhibits higher CO_2 adsorption capacity compared to MOF-808-PEI and COF-CHO (Fig. 4b). In other words, the MOF core ensures a high surface area scaffold, the reorganized PEI shell provides a dense yet accessible population of chemisorption sites, and the COF outer shell maintains accessibility while suppressing water interference. This structural hierarchy directly translates into the superior CO_2 uptake and stability observed for CSS-PEI compared with either component alone.

To achieve the highest adsorption capacity of the CSS nanocomposites, samples with various amounts of PEI loading on the shell pore wall were prepared. As shown in Fig. 3d, CSS-*X*% (*X* = 25, 50, 75, 100, implying *X* percentage of PEI loading) samples were synthesized

https://doi.org/10.1038/s41467-025-65531-3

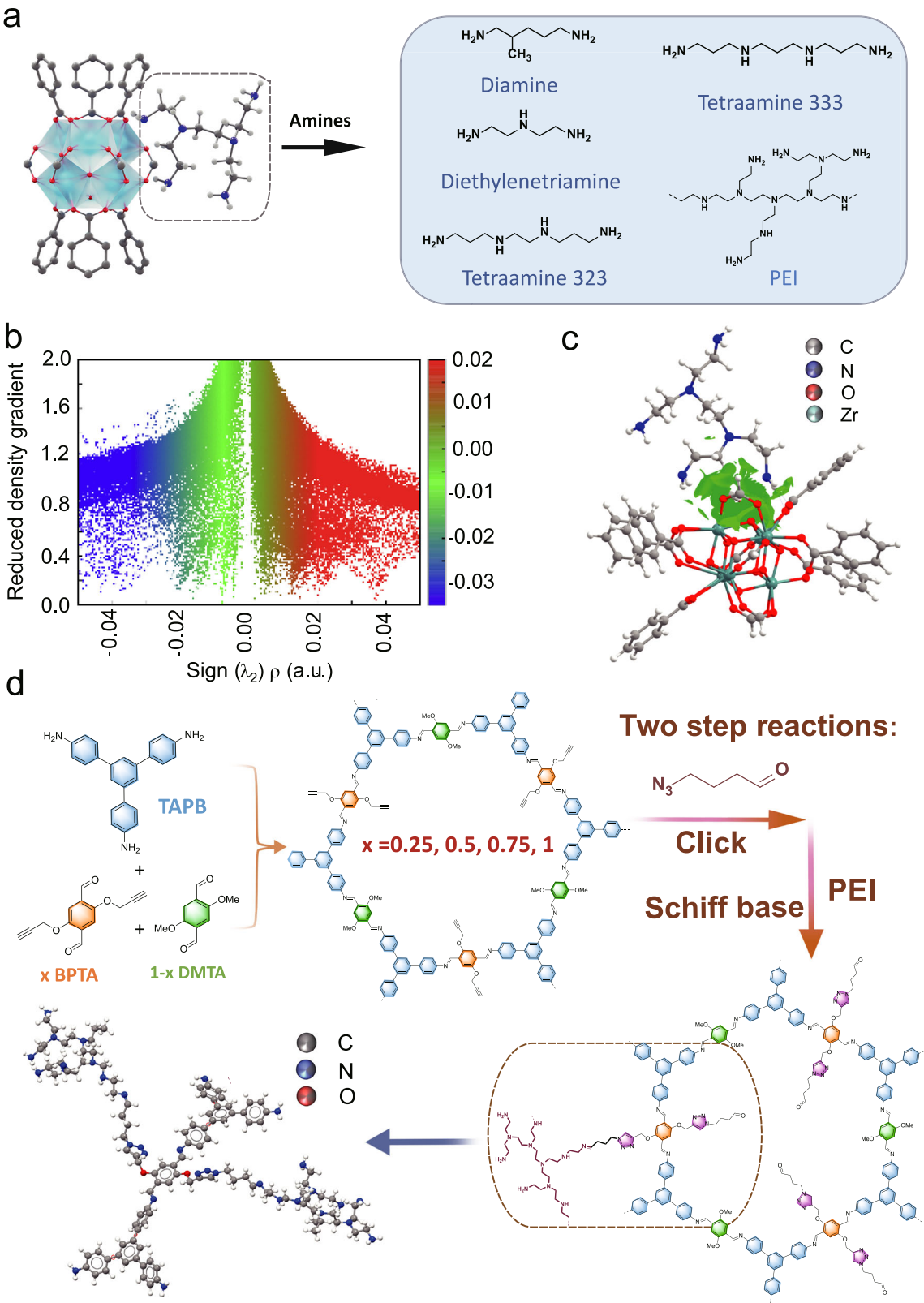

Fig. 3 | Optimization of amine functionalization in the MOF core and COF shell. **a** Optimization of CO_2 adsorption capacity in MOF-808 using various amines. **b** Non-covalent interactions of MOF-808-PEI, analyzed using an independent gradient model based on Hirshfeld partition (IGMH) with isosurface of reduced density gradient (RGD) = 0.5 (blue denoted strong attractions, including hydrogen bonding, green indicated van der Waals interactions, and red represented strong repulsion, including steric hindrance). **c** DFT-optimized structure of MOF-808-PEI. **d** Functionalization of the COF shell and the optimized structure of a COF-PEI fragment. The degree of functionalization was controlled by adjusting the ratio of BPTA/DMTA ligands, followed by sequential click and Schiff-base reactions to achieve precise amine incorporation.

https://doi.org/10.1038/s41467-025-65531-3

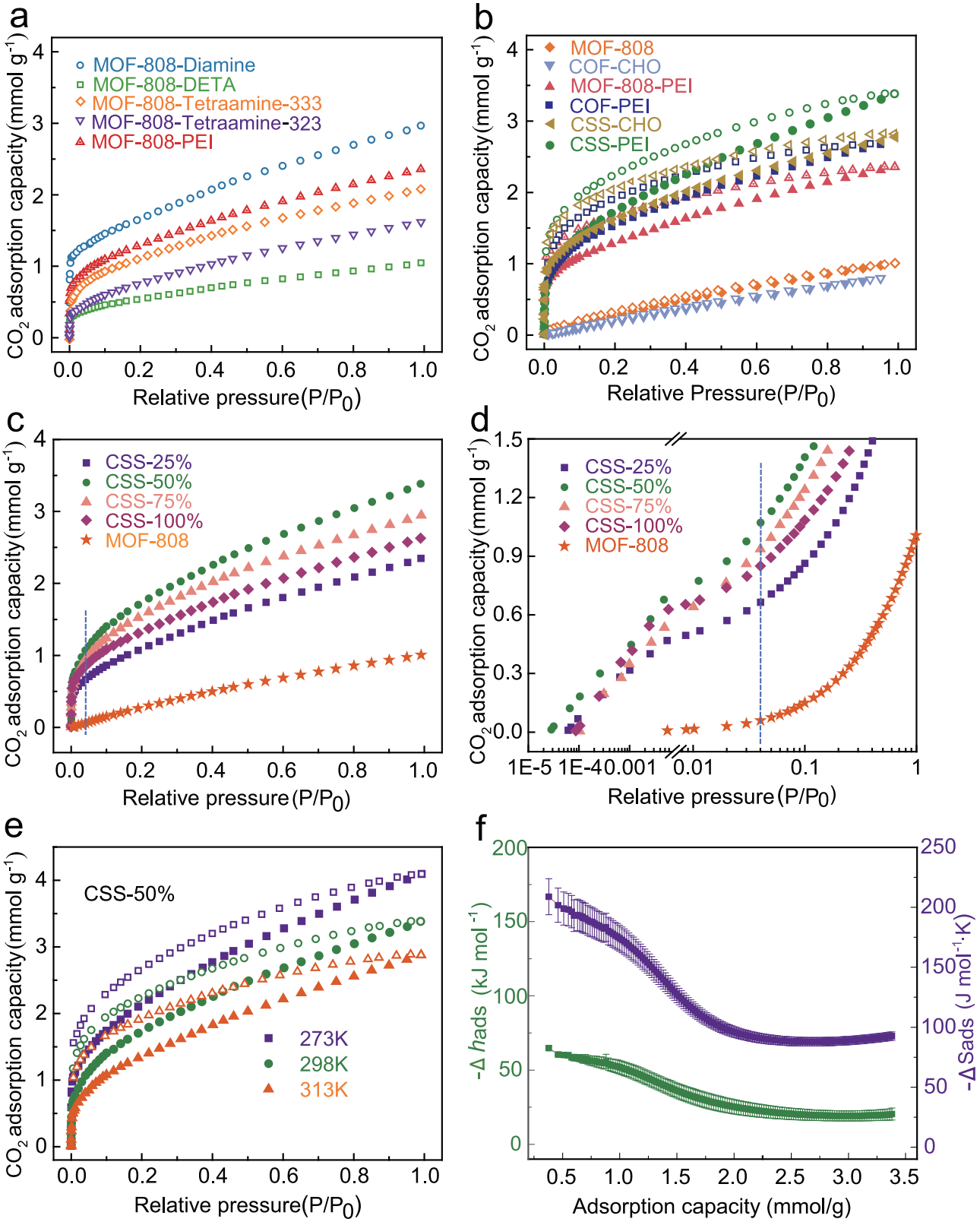

Fig. 4 | CO_2 adsorption isotherms. a CO_2 adsorption isotherms of MOF-808 with Diamine (MDPA), DETA, tetramine and PEI. **b** CO_2 adsorption isotherms of MOF-808, MOF-808-PEI, COF-PEI, CSS-CHO and CSS-PEI. **c** CO_2 adsorption isotherms of CSS-25%, CSS-50%, CSS-75% and CSS-100%. **d** Zoomed in CO_2 adsorption isotherms at relative pressure of 0.04. **e** CO_2 adsorption isotherms of CSS-50% at 273, 298 and 313 K. **f** $-\Delta h_{ads}$ (enthalpy) and $-\Delta s_{ads}$ (entropy) for CSS-50% determined using the Clausius–Clapeyron equation as a function of CO_2 loading. The blue dashed lines in Fig. 4c, d indicate the CO_2 partial pressure in flue gas. Error bars were obtained from the standard errors derived through linear regression fit.

by varying the ratio of the COF edge ligand. Comparison of the isotherms (Fig. 4c and Supplementary Fig. 18) showed that CSS-50% has the best CO_2 capacity of 3.4 mmol g^{-1} at 1 bar. The decreased CO_2 adsorption capacity for CSS-75% and CSS-100% was attributed to the overloading of bulky PEI which blocks the pore of the COF shell, as evidenced by the N_2 adsorption isotherms where the surface area decreased with an order of CSS-25% <CSS-50% <CSS-75% <CSS-100% (Supplementary Fig. 14). Additionally, a significant hysteresis between the adsorption curve and desorption curve was observed (Fig. 4b), characteristic of CO_2 chemisorption, which was not fully reversible at 25 °C. This phenomenon was observed for other amine-modified samples and was absent for MOF-808. This eliminates the possibility of having any unoccupied sites (open metal sites) in the MOF backbone contributing to the observed strong adsorption. Notably, CSS-50% absorbs 1.07 mmol g^{-1} at 40 mbar CO_2 (relevant to post-combustion capture from natural gas flue gas), an 18-fold increase compared to that of MOF-808, which absorbs 0.059 mmol g^{-1} at the same pressure (Fig. 4d). At 400 mbar, CSS-50% absorbs 2.1 mmol g^{-1} CO_2, a 53-fold increase from MOF-808. While the adsorption capacity is slightly lower than the benchmark adsorbent Zeolite 13× (1.07 mmol g^{-1} at 5.5×10^{-3} bar)[27], CSS-50% offers improved performance under humid conditions due to its hydrophobic nature. The COF shell in the CSS nanocomposites acts as a diffusion barrier to water vapor, leading to a 65% reduction in H_2O adsorption for CSS-50% (Supplementary Fig. 19, 250 $cm^3 g^{-1}$ at $P/P_0 = 0.8$) compared to MOF-808[25], thus favoring selective CO_2 capture under humidity. Although CALF-20, another benchmark sorbent for industrial-scale CO_2 capture, exhibits a higher CO_2 capacity of 2.6 mmol g^{-1} at 0.15 bar[28], its physisorption mechanism limits its effectiveness in high-humidity environments.

Humidity tolerance and adsorption mechanism

DOE's goal for capturing 90% of CO_2 from natural gas flue stream (~4% CO_2) prompted the analysis of CO_2 adsorption and desorption isotherms for CSS-50% at 273, 298, and 313 K (Fig. 4e). At these conditions, achieving 90% CO_2 adsorption efficiency (e.g., removal from 40 to 4 mbar at atmosphere pressure) is readily accomplished. The differential adsorption enthalpy (Δh_{ads}) and entropy (Δs_{ads}) were calculated to be 52 ± 4 kJ mol^{-1} and 174 ± 10 J mol^{-1} K, respectively, at a CO_2 adsorption capacity of 1 mmol CO_2 g^{-1} based on the Clausius–Clapeyron equation (Fig. 4f and Supplementary Fig. 20). The Δs_{ads} value is slightly lower than that of MOF-274[29], which is expected due to the coexistence of chemisorption and physisorption in the CSS-PEI samples (Supplementary Fig. 21). Notably, the enthalpy of adsorption (52 kJ mol^{-1}) is nearly half that of amine-appended MOF-274[29], indicating that the nanocomposites are likely to require lower regeneration energy compared to amine-functionalized MOFs. Additionally, the variation in Δh_{ads} with increasing adsorption capacity indicates interactions between CO_2 adsorption sites as capacity increases. These interactions may influence the overall adsorption dynamics and efficiency, highlighting the complex nature of CO_2 adsorption in these nanocomposites.

The significant increase in CO_2 adsorption capacity provided strong evidence that the introduction of strong chemisorption sites through incorporating polyamines into COF holds promise for practical applications. Since most scenarios involve feed streams containing water, it is crucial to evaluate the CO_2 adsorption capacity of CSS-PEI in the presence of humidity. We thus tested CSS-50% in a dynamic breakthrough system, where an activated sample was first saturated in a mixture of 79% N_2 and 21% O_2 with a relative humidity (RH) of 60% at 25 °C and 1 atm and was then exposed to a mixture of 0.04% (400 ppm) CO_2, 79% N_2, and 21% O_2 with an RH of 60% at 25 °C and 1 atm. Numerical integration of the monitored concentrations revealed that the CO_2 adsorption capacity of CSS-50% from 400 ppm CO_2 in the presence of 60% RH at 25 °C and 1 atm was 0.83 mmol g^{-1} (Supplementary Fig. 22).

To investigate the CO_2 adsorption mechanism of CSS-50% in both dry and humid conditions, we conducted solid-state cross-polarization magic-angle spinning (CP-MAS) ^{13}C NMR experiments. These tests were performed on the representative CSS-50% variant to analyze the chemical changes before and after exposure to $^{13}CO_2$, with and without the presence of water (Fig. 5a). First, the CSS-PEI sample was placed in a rotor and dosed with 0.97 bar of $^{13}CO_2$ at 25 °C, after which CP-MAS SSNMR measurements were repeated. The resulting spectra showed a weak signal around 135 ppm, corresponding to aromatic carbon from the CSS nanocomposites linkage. Two distinct signals were observed at δ ^{13}C = 164 and 168.8 ppm, indicating the formation of carbamate (-NHCOO-) species through covalent interaction between CO_2 and primary amines[29]. These two signals suggest the presence of different chemical environments for chemisorbed CO_2, likely due to multiple amines within a single PEI molecule, leading to varied interactions. For comparison, a fully activated CSS-50% sample was humidified by exposure to 95% RH in a N_2 atmosphere at 1 atm and 25 °C for 24 h. The sample was then exposed to 0.9 bar of $^{13}CO_2$ for 24 h, followed by CP-MAS SSNMR measurements under the same conditions as the dry sample. The resulting ^{13}C NMR spectrum revealed a similar carbamate signal at δ ^{13}C = 164 ppm. However, the signal at 168.8 ppm shifted to 167 ppm, indicating that H_2O participated in the adsorption process. We thus conclude that the predominant chemisorption product is ammonium carbamate.

Cycling durability and chemical stability

To further evaluate the durability of CSS nanocomposites under flue gas capture conditions, CO_2 capacity was measured under humid CO_2 (15%) at 40 °C for 100 consecutive adsorption-desorption cycles. As shown in Fig. 5b, the normalized CO_2 adsorption capacity of CSS-PEI remained stable, whereas MOF-808-PEI exhibited a 20% decline (Supplementary Fig. 23), highlighting the enhanced cycling stability of CSS nanocomposites. To explore the cause of this difference, we hypothesize that the MOF-808-PEI sample undergoes amine loss during repeated adsorption-desorption cycles. To test this hypothesis, FT-IR experiments were conducted before and after CO_2 adsorption-desorption cycles. Results indicated that in the absence of a COF shell, N-H stretching at 3200–3500 cm^{-1} diminished (Supplementary Fig. 24), suggesting a decrease in PEI loading after cycling. In contrast, CSS-PEI exhibited no significant spectral changes (Supplementary Fig. 25), suggesting a negligible loss of PEI due to strong covalent bonding. This highlights how the covalent anchoring of PEI by the COF shell, combined with the porous reorganization of the interfacial mesh, preserves both the chemical functionality and adsorption capacity through repeated cycling-an outcome that cannot be achieved by the MOF core or PEI alone. Additionally, the adsorption kinetics of CSS-PEI and MOF-808-PEI were measured under 15% CO_2 across a temperature range of 40–70 °C (Supplementary Figs. 26–29 and Tables 2–3). As shown in Supplementary Fig. 26, CSS nanocomposite reached half capacity within 4 min at 40 °C, the adsorption rate was increased with temperature and followed Arrhenius behavior, consistent with other amine-appended solid sorbents[30].

We further compared the chemical stabilities of MOF-808 and CSS nanocomposites by immersing them in various solvents for 1 week, including 3 M HNO_3 solution and NaOH solution (PH = 14). The residual weight percentage of these samples is presented in Fig. 5e. In the tested organic solvents, both MOF-808 and CSS nanocomposites exhibited minimal weight loss (<0.1 wt%). Under acidic (3 M HNO_3) and basic (NaOH aqueous solution, pH = 14) conditions, the residual weight percentages were approximately 99 wt% for CSS nanocomposites, whereas MOF-808 demonstrated approximately 87 wt% remaining for acidic conditions and 72 wt% remaining for basic conditions. Additionally, CSS nanocomposites maintained its original crystalline structure, as evidenced by the unchanged intensities and positions of the peaks in the PXRD patterns (Fig. 5c and Supplementary Fig. 30).

https://doi.org/10.1038/s41467-025-65531-3

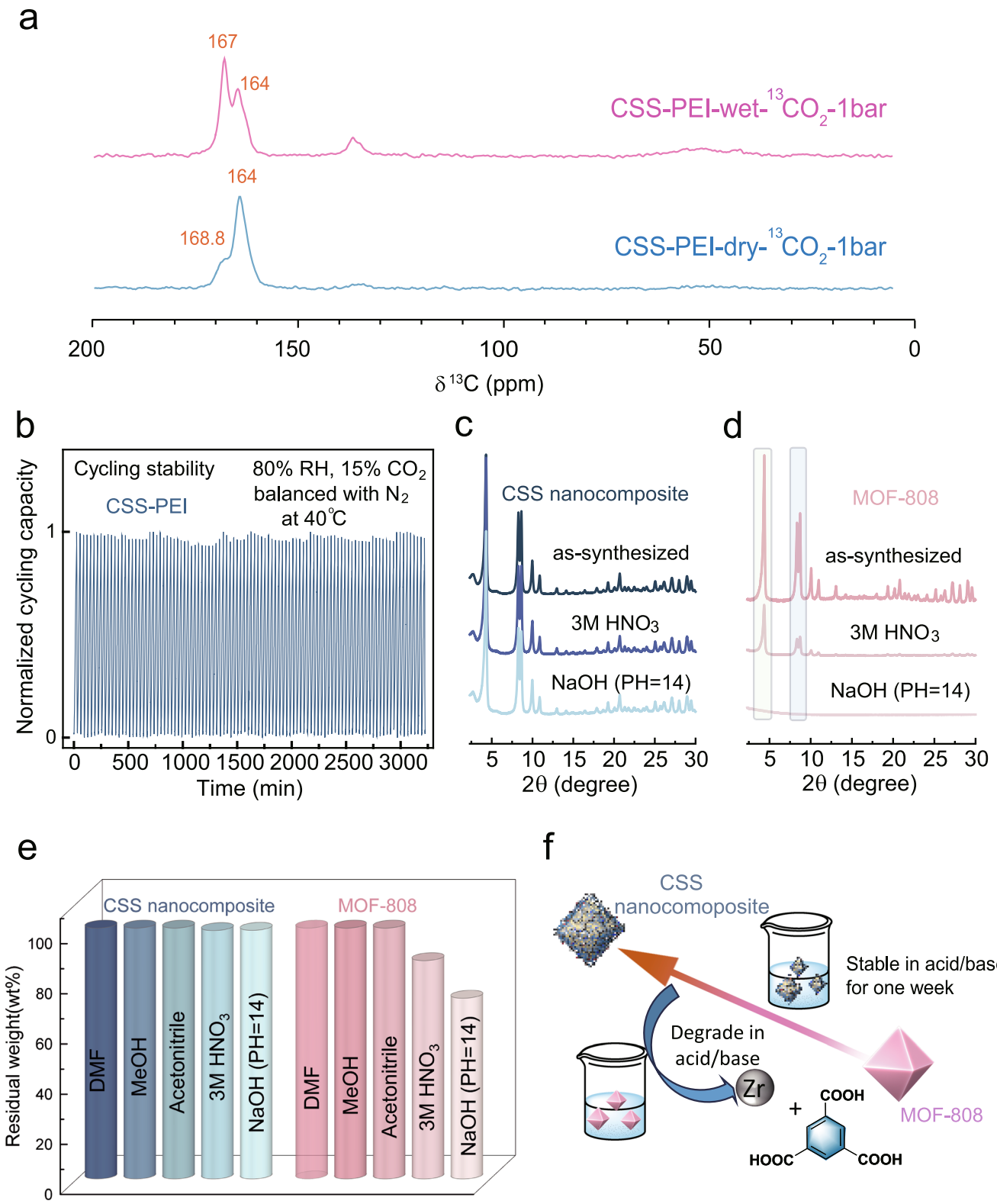

Fig. 5 | Evaluation of CO_2 adsorption performance and chemical stability of CSS nanocomposites. a Cross-polarized ^{13}C MAS NMR spectra of CSS-50% exposed to 0.9 bar dry and wet $^{13}CO_2$. Two peaks at 164 and 168.8 ppm correspond to carbamate species. The peak shift observed under wet condition indicates the participation of H_2O in the adsorption process. **b** Normalized CO_2 adsorption capacity of CSS-PEI over 100 adsorption-desorption cycles under humid conditions (15% CO_2, 40 °C) using a custom dosing setup, demonstrating stable performance. **c**, **d** PXRD patterns of MOF-808 and CSS nanocomposites after soaking in acidic and basic solution for 1 week. While MOF-808 showed a loss of crystallinity (reduced peak intensities), the CSS nanocomposites retained their structural integrity. **e** Residue weight percentage of CSS nanocomposites and MOF-808 after treatment for 1 week in different solvents. **f** Schematic illustration of the chemical stability of CSS nanocomposites and MOF-808.

Conversely, the peak intensity of MOF-808 decreased after immersion in the 3 M HNO_3 solution, and it completely lost crystallinity in the NaOH solution (Fig. 5d). To assess the impact on CO_2 adsorption performance, we compared the CO_2 adsorption capacity of CSS nanocomposites and MOF-808 after chemical treatment (Supplementary Figs. 31 and 32). While CSS nanocomposites maintained their adsorption capacity, MOF-808 exhibited a noticeable decline, likely due to the loss of their crystallinity. The superior chemical stability of CSS nanocomposites was attributed to the inherent ultra-stability provided by the COF shell, which is reinforced by electron density delocalization of the two long pairs of methoxy groups, stabilizing the structure[26]. Furthermore, the COF shell enhances the hydrophobicity of the hybrids, as evidenced by an increase in the contact angle of CSS-PEI from 35° to 55° compared to MOF-808 (Supplementary Fig. 33). This enhanced hydrophobicity restricts water diffusion, thereby improving chemical stability under harsh conditions. Moreover, this restriction prevents competitive bonding between water and CO_2, thus enhancing selective CO_2 adsorption even in humid environments.

In conclusion, we have developed a new strategy that employs a dual-amine functionalized CSS architecture for efficient CO_2 capture. As a proof of concept, we synthesized CSS nanocomposites through the cooperative assembly of COF and polyamines on a MOF core. This approach leverages COF as effective diffusion barriers against water vapor and offers dual adsorption sites, delivering enhanced stability and suitability for CO_2 capture in realistic flue gas conditions. Taking advantage of the molecular-level dual amine functionalization through strong covalent bonding, we have demonstrated that the nanocomposites exhibited an improved CO_2 adsorption capacity of 3.4 mmol g^{-1} at 1 bar with low regeneration energy. Additionally, with adsorption capacities of 1.07 mmol g^{-1} at 40 mbar and 2.1 mmol g^{-1} at 400 mbar, they demonstrate considerable potential for direct air capture. More broadly, our results establish a clear structure-activity relationship: the MOF core contributes intrinsic porosity, the CSS structure generates dual chemisorption sites, and the COF shell stabilizes and protects these functionalities under harsh conditions. The integration of these complementary roles is the key driver of the exceptional CO_2 capture performance. Future efforts to apply this strategy across other solid sorbents could unlock a diverse range of amine-functionalized CSS porous crystalline materials, advancing carbon capture technology with enhanced performance, stability, and efficiency.

Methods

Instrumentation and general characterization

FT-IR spectra were recorded using PerkinElmer Spectrum One FT-IR. PXRD patterns were recorded with Rigaku MiniFlex 6 G Benchtop XRD, using Cu $K\alpha_1$ radiation ($\lambda = 1.5406$ Å). TGA was conducted on a TA Instruments Q5500 under N_2 atmosphere, heating to 600 °C at a rate of 10 °C min^{-1}. CO_2 adsorption kinetics were measured with approximately 5–10 mg samples between 40 and 70 °C under dry 15% CO_2 at a flow rate of 25 mL/min. Leaching experiments were performed by immersing 10 mg of the sample in 1 mL of D_2O for 3 h, followed by the collection of the supernatant and analysis by ^1H NMR spectroscopy. Water adsorption isotherm were obtained using ASAP 2020 analyzer (Micromeritics) with water vapor accessory; samples were activated under 120 °C overnight before measurement; the water vapor source was degassed through three freeze-pump-thaw cycles. XPS was carried out using a Thermo Scientific™ K-Alpha Plus™ system with monochromatic Al Kα radiation (1486.7 eV) as the excitation source. Nitrogen sorption isotherms were obtained at 77 K using a liquid nitrogen bath with an ASAP 2020 analyzer (Micromeritics). The Brunauer-Emmett-Teller (BET) method was utilized to calculate the surface area; pore size distribution was derived from the sorption curve by using QSDFT model.

Synthesis of MOF-808-PEI

MOF-808 was prepared according to the procedure given in the literature[25]. To a 20 ml glass vial, MOF-808 (100 mg), PEI (50 mg, average MW ~ 800), PVP (50 mg) and methanol (15 mL) were added and stirred at room temperature overnight to yield a white solid. The white solid was isolated by centrifugation (11180 g) and washed with methanol 3 times. Drying under N_2 yielded MOF-808-PEI as a white solid (98 mg, 98% yield).

Synthesis of CSS nanocomposites

CSS-C≡CH. A 30 ml glass vial was charged with MOF-808-PEI (20 mg), 2,5-bis(2-propynyloxy)terephthalaldehyde (4.8 mg, 0.02 mmol), 1,3,5-tri-(4-aminophenyl)benzene (4.8 mg, 0.014 mmol), glacial acetic acid (200 µL) and anhydrous acetonitrile (20 ml). After ultrasonication via Ultrasonic Cleaners (VWR model 250D) for 30 min, the mixture was maintained at room temperature for another 4 h. Afterwards, 800 µL of acetic acid was further added, and the mixture was heated at 80 °C for 24 h in an oven to yield a yellow solid. The yellow solid (27 mg, 91.2% yield) was obtained by centrifugation (11180 g) after washing with methanol and acetone 3 times. CSS-*X*% (*X* represents the percentage of functional groups, either of -C≡CH or PEI) was obtained via the same method described above, except using the combination of 2,5-bis(2-propynyloxy)terephthalaldehyde and 2,5-dimethoxyterephthalaldehyde (a total of 0.02 mmol) at different molar ratios of 3/1, 1/1, 1/3 to manipulate the amount of functional groups.

CSS-CHO. A 20 ml Biotage microwave vial was charged with CSS-C≡CH (100 mg), CuI (10 mg), 4-azidobutanal in CH_2Cl_2 (50% by wt%, 50 mg, 0.22 mmol), N, N-diisopropylethylamine (0.2 mL), toluene (4 mL) and n-butanol (1 mL). The mixture was flash frozen 3 times at 77 K in a liquid nitrogen bath. After warming to room temperature, the mixture was stirred for 2 days. After washing with methanol and acetone for 3 times, the product was obtained by centrifugation (11180 g) as a yellow solid (113 mg, 98.1% yield).

CSS-PEI. CSS-CHO (20 mg), ethanol (15 mL) and an excess amount of PEI (average MW ~ 800) were added to a 20 ml glass vial. The mixture was stirred at 45 °C overnight to ensure complete reaction. The product was obtained by centrifugation (11180 g) after washing with methanol and acetone 3 times as a yellow solid. The solid collected was dried at room temperature under vacuum overnight to give a yellow powder (19 mg, 95% yield).

DFT calculations

DFT calculations were carried out with the Gaussian 09 program package[31]. The geometry optimizations were performed using the dispersion-corrected B3LYP[32,33] functional with Grimme's D3 dispersion correction[34], with a mixed basis set of LANL2DZ basis set[35,36] for Zr and 6-31 G(d) basis set[37] for other atoms. This theoretical level is denoted as B3LYP-GD3BJ/6-31 G(d), LANL2DZ(Zr). The reduced density gradient isosurface in the NCI method[38] were performed by using the Multiwfn 3.7 software[39], to get an insight of intermolecular interactions.

CO_2 adsorption isotherms

CO_2 adsorption isotherms were measured using an ASAP 2020 analyzer (Micromeritics) at 278, 298, and 313 K, with CO_2 as the adsorbate. Prior to measurements, the samples were degassed under vacuum at 85 °C overnight. Approximately 30–40 mg of the degassed sample was weighed and loaded into the analyzer tube. Equilibrium was defined as a weight change of less than 0.001% over a 30 s interval.

Cycling experiment

Cycling experiments were conducted using a TA Instruments Q5500. Approximately 5 mg of sample was activated at 120 °C for 30 min

under N_2 prior to measurement. Adsorption was conducted at 40 °C under a 15% CO_2/N_2 mixture (balanced with N_2) at 80–85% RH and a total flow rate of 25 mL min^{-1}. During adsorption, the temperature was decreased to 40 °C at a rate of 5 °C min^{-1} and held for 10 min to ensure complete CO_2 uptake. Desorption was then performed by heating to 120 °C at a ramp rate of 20 °C min^{-1} and holding for 10 min.

Breakthrough

Adsorption breakthrough experiments were conducted using a home-built setup. Approximately 0.5 g of samples were used to prepare pellets and activated under a 30 sccm He flow at 140 °C for 30 min. Following activation, breakthrough measurements were performed with 466.6 mg of sample under a feed of 400 ppm CO_2 at 60% RH.

Cryo-EM analysis

A 4 µl aliquot of the sample solution was applied to a glow-discharged, ultra-thin carbon film grid (200 mesh copper, CF200-Cu-UL, Electron Microscopy Sciences, Hatfield, PA, USA). The grid was air-dried and stored in liquid nitrogen for cryo-EM Imaging. Imaging was performed using a Titan Krios G3i transmission electron microscope (Thermo Fisher Scientific) equipped with a Bioquantum energy filter (Gatan Inc., Pleasanton, CA, USA), operated at 300 keV. Micrographs were acquired using a Gatan K3 direct electron detector in correlated double sampling mode[40] and super-resolution mode, controlled by SerialEM[41].

The micrographs were acquired at a nominal magnification of 53 k× (0.835 Å/pixel) with 50 frames and a total electron dose of ~50 $e^-/Å^2$. Motion correction of the multi-frame images was performed using MotionCor2[42]. The contrast transfer function (CTF) was determined, and phase flipped using GCTF software[43]. The micrographs were analyzed via fast Fourier transform (FFT) and processed with a Wiener filter[44] in Gatan Digital Micrograph software.

Data availability

All data generated or analyzed during this study are included in paper and its Supplementary Information. Source data are provided with this paper.

References

1. Solomon, S., Plattner, G. K., Knutti, R. & Friedlingstein, P. Irreversible climate change due to carbon dioxide emissions. *Proc. Natl. Acad. Sci. USA* **106**, 1704–1709 (2009).
2. Service, R. F. Energy carbon capture marches toward practical use. *Science* **371**, 1300–1300 (2021).
3. Global CCS Institute, 2023 Global status of CCS report. (Global CCS Institute, 2023).
4. Bui, M. et al. Carbon capture and storage (CCS): the way forward. *Energy Environ. Sci.* **11**, 1062–1176 (2018).
5. Congressional research service, carbon capture and sequestration (CCS) in the United States. (Congressional Research Service, 2022).
6. Singh, G. et al. Emerging trends in porous materials for CO_2 capture and conversion. *Chem. Soc. Rev.* **49**, 4360–4404 (2020).
7. Dutcher, B., Fan, M. H. & Russell, A. G. Amine-based CO_2 capture technology development from the beginning of 2013-A review. *ACS Appl. Mater. Interfaces* **7**, 2137–2148 (2015).
8. Dunstan, M. T., Donat, F., Bork, A. H., Grey, C. P. & Müller, C. R. CO_2 capture at medium to high temperature using solid oxide-based sorbents: fundamental aspects, mechanistic insights, and recent advances. *Chem. Rev.* **121**, 12681–12745 (2021).
9. Creamer, A. E. & Gao, B. Carbon-based adsorbents for post-combustion CO_2 capture: a critical review. *Environ. Sci. Technol.* **50**, 7276–7289 (2016).
10. Yang, Y., Li, H. C., Chen, S. X., Zhao, Y. N. & Li, Q. H. Preparation and characterization of a solid amine adsorbent for capturing CO_2 by grafting allylamine onto PAN fiber. *Langmuir* **26**, 13897–13902 (2010).
11. Choi, S., Drese, J. H. & Jones, C. W. Adsorbent materials for carbon dioxide capture from large anthropogenic point sources. *Chemsuschem* **2**, 796–854 (2009).
12. Li, G. et al. Capture of CO_2 from high humidity flue gas by vacuum swing adsorption with zeolite 13X. *Adsorption* **14**, 415–422 (2008).
13. Li, H. et al. Recent advances in gas storage and separation using metal-organic frameworks. *Mater. Today* **21**, 108–121 (2018).
14. Trickett, C. A. et al. The chemistry of metal-organic frameworks for CO_2 capture, regeneration and conversion. *Nat. Rev. Mater.* **2**, 17045 (2017).
15. Song, K. S., Fritz, P. W. & Coskun, A. Porous organic polymers for CO_2 capture, separation and conversion. *Chem. Soc. Rev.* **51**, 9831–9852 (2022).
16. McDonald, T. M. et al. Cooperative insertion of CO_2 in diamine-appended metal-organic frameworks. *Nature* **519**, 303–308 (2015).
17. Kim, E. J. et al. Cooperative carbon capture and steam regeneration with tetraamine-appended metal-organic frameworks. *Science* **369**, 392–396 (2020).
18. Shi, X. Y. et al. Water-stable MOFs and hydrophobically encapsulated MOFs for CO_2 capture from ambient air and wet flue gas. *Mater. Today* **65**, 207–226 (2023).
19. McDonald, T. M. et al. Capture of carbon dioxide from air and flue gas in the alkylamine-appended metal-organic framework mmen-Mg_2(dobpdc). *J. Am. Chem. Soc.* **134**, 7056–7065 (2012).
20. Milner, P. J. et al. Overcoming double-step CO_2 adsorption and minimizing water co-adsorption in bulky diamine-appended variants of Mg_2(dobpdc). *Chem. Sci.* **9**, 160–174 (2018).
21. Lyu, H. et al. Covalent organic frameworks for carbon dioxide capture from air. *J. Am. Chem. Soc.* **144**, 12989–12995 (2022).
22. Zhou, Z. et al. Carbon dioxide capture from open air using covalent organic frameworks. *Nature* **635**, 96–101 (2024).
23. Huang, N., Chen, X., Krishna, R. & Jiang, D. L. Two-dimensional covalent organic frameworks for carbon dioxide capture through channel-wall functionalization. *Angew. Chem., Int. Ed.* **54**, 2986–2990 (2015).
24. Kalaj, M. et al. MOF-polymer hybrid materials: from simple composites to tailored architectures. *Chem. Rev.* **120**, 8267–8302 (2020).
25. Furukawa, H. et al. Water adsorption in porous metal-organic frameworks and related materials. *J. Am. Chem. Soc.* **136**, 4369–4381 (2014).
26. Xu, H., Gao, J. & Jiang, D. L. Stable, crystalline, porous, covalent organic frameworks as a platform for chiral organocatalysts. *Nat. Chem.* **7**, 905–912 (2015).
27. Lee, J.-S. et al. Adsorption equilibria of CO_2 on zeolite 13X and zeolite X/activated carbon composite. *J. Chem. Eng. Data.* **47**, 1237–1242 (2002).
28. Lin, J.-B. et al. A scalable metal-organic framework as a durable physisorbent for carbon dioxide capture. *Science* **374**, 1464–1469 (2021).
29. Forse, A. C. et al. Elucidating CO_2 chemisorption in diamine-appended metal-organic frameworks. *J. Am. Chem. Soc.* **140**, 18016–18031 (2018).
30. Monazam, E. R., Shadle, L. J. & Siriwardane, R. Equilibrium and absorption kinetics of carbon dioxide by solid supported amine sorbent. *AIChE J.* **57**, 3153–3159 (2011).
31. Frisch, M. J. et al. *Gaussian 09, Revision C.01* (Gaussian, Inc., 2010).
32. Becke, A. D. Density-functional thermochemistry. III. the role of exact exchange. *J. Chem. Phys.* **98**, 5648–5652 (1993).
33. Lee, C., Yang, W. & Parr, R. G. Development of the colle-salvetti correlation-energy formula into a functional of the electron density. *Phys. Rev. B* **37**, 785–789 (1988).
34. Grimme, S., Antony, S., Ehrlich, S. & Krieg, S. A consistent and accurate ab initio parametrization of density functional dispersion correction (DFT-D) for the 94 elements H-Pu. *J. Chem. Phys.* **132**, 154104 (2010).

35. Wadt, W. R. & Hay, P. J. Ab initio effective core potentials for molecular calculations. Potentials for main group elements Na to Bi. *J. Chem. Phys.* **82**, 284–298 (1985).
36. Hay, P. J. & Wadt, W. R. Ab initio effective core potentials for molecular calculations. Potentials for the transition metal atoms Sc to Hg. *J. Chem. Phys.* **82**, 270–283 (1985).
37. Woon, D. E. & Dunning, T. H. Gaussian basis sets for use in correlated molecular calculations. V. core-valence basis sets for boron through neon. *J. Chem. Phys.* **103**, 4572–4585 (1995).
38. Johnson, E. R. et al. Revealing noncovalent interactions. *J. Am. Chem. Soc.* **132**, 6498 (2010).
39. Lu, T. & Chen, F. Multiwfn: a multifunctional wavefunction analyzer. *J. Comput. Chem.* **33**, 580–592 (2012).
40. Sun, M. et al. Practical considerations for using K3 cameras in CDS mode for high- resolution and high-throughput single particle cryo-EM. *J. Struct. Biol.* **213**, 107745 (2021).
41. Mastronarde, D. N. Automated electron microscope tomography using robust prediction of specimen movements. *J. Struct. Biol.* **152**, 36–51 (2005).
42. Zheng, S. Q. et al. MotionCor2: anisotropic correction of beam-induced motion for improved cryo-electron microscopy. *Nat. Methods* **14**, 331–332 (2017).
43. Zhang, K. Gctf: real-time CTF determination and correction. *J. Struct. Biol.* **193**, 1–12 (2016).
44. Kilaas, R. Optimal and near-optimal filters in high-resolution electron microscopy. *J. Microsc.* **190**, 45–51 (1998).

Acknowledgements

Work at the Molecular Foundry was supported by the Office of Science, Office of Basic Energy Sciences, U.S. Department of Energy, under Contract No. DE-AC02-05CH11231. This work was partly supported by the Department of Energy (DOE), Office of Basic Energy Sciences, Division of Materials Sciences and Engineering (contract no. DE-AC02-76SF00515). J.A.R. acknowledges partial support from the PrISMa Project (299659), funded through the ACT Programme (Accelerating CCS Technologies, Horizon 2020 Project 294766). D.M.H. acknowledges support from the Joint Center for Energy Storage Research, an Energy Innovation Hub funded by the U.S. Department of Energy, Office of Science, Basic Energy Science. We thank Panagiotis Reskos for calculating molecular and complex structures. We also thank Dr. Hasan Celik, Dr. Raynald Giovine and the College of Chemistry NMR Facility, University of California, Berkeley. J.L. and G.R. were partially supported by funds from US National Institutes of Health grants (R01HL115153, R01MH077303 and R01DK042667).

Author contributions

J.U., Y.C., and J.A.R. supervised the project. H.M., S.Y., and C. D., conceived the idea. Y.C., J.A.R., J.U., H.M., and S.Y. planned the study, designed the experiments, analyzed the data and composed the manuscript. S.Y. and H.M. and all others conducted the experiments. J.L. and G.R. carried out the cryo-EM analysis. K.H., A.C., and X.Z. performed the XPS measurements. J.K.L. and D.L. conducted the TGA measurements. H.L., Z.C., and X.X. measured the contact angles. X.L. and H.Z. collected the H_2O adsorption isotherms. J.R.L. contributed to the fruitful discussion and gave valuable suggestions. All the authors reviewed and commented on the manuscript.

Competing interests

The authors declare no competing interests.

Additional information

Supplementary information The online version contains supplementary material available at https://doi.org/10.1038/s41467-025-65531-3.

Correspondence and requests for materials should be addressed to Jeffrey A. Reimer, Yi Cui or Jeffrey J. Urban.

Peer review information *Nature Communications* thanks Haijun Zhang, and the other, anonymous, reviewer(s) for their contribution to the peer review of this work. A peer review file is available.